International Journal of Impact Engineering 159 (2022) 104035

Contents lists available at ScienceDirect

International Journal of Impact Engineering

journal homepage: www.elsevier.com/locate/ijimpeng

Enhanced ballistic resistance of multilayered cross-ply UHMWPE laminated plates

Rui Zhang [a,b,c], Bin Han [b,*], Jun-Yang Zhong, Methodology [a,c], Lu-Sheng Qiang [c,d], Chang-Ye Ni, Software [c,d], Qi Zhang, Resources [b], Qian-Cheng Zhang, Project administration [a], Bin-Chao Li, Project administration [e], Tian Jian Lu [c,d,*]

[a] State Key Laboratory for Strength and Vibration of Mechanical Structures, Xi'an Jiaotong University, Xi'an 710049, PR China
[b] School of Mechanical Engineering, Xi'an Jiaotong University, Xi'an 710049, PR China
[c] State Key Laboratory of Mechanics and Control of Mechanical Structures, Nanjing University of Aeronautics and Astronautics, Nanjing 210016, PR China
[d] MIIT Key Laboratory of Multi-functional Lightweight Materials and Structures, Nanjing University of Aeronautics and Astronautics, Nanjing 210016, PR China
[e] Xi'an Aerospace Propulsion Institute, Xi'an 710100, PR China

ARTICLE INFO

Keywords:
Polymeric composites
Ballistic resistance
Multilayer plates
Experiment

ABSTRACT

Multilayered cross-ply ultra-high molecular weight polyethylene (UHMWPE) laminated plates were envisioned and their ballistic performance explored, both experimentally and numerically. High velocity impacts were performed on both monolithic and multilayered targets with identical areal density. Ballistic data were obtained, together with dynamic deformation features and failure modes for both target types. Full three-dimensional finite element (FE) simulations were carried out to calculate the dynamic response of each target and explore the underlying mechanisms. Good agreement was achieved between FE simulations and experimental measurements. The results revealed that multi-layering the target could relieve fiber tensile stresses on its rear face and generate a more significant pull-in effect at the edges, resulting in larger back-face deflection and enhanced ballistic resistance.

1. Introduction

The ballistic performance of protective structures subjected to projectile impact has long been of interest in both military and civilian applications. To meet the increasing demand of lightweight, the design of a protective structure was no longer limited to a single material or a single layer. As a potential improvement over monolithic plates, multilayered constructions have been envisioned, with no bonding between adjacent layers [1]. The penetration response of such multilayered targets has therefore become important for protection design.

The ballistic performance of multilayered metallic plates has been extensively investigated. For typical instance, the residual velocity of a double-layered aluminum plate was found to be comparable to that of a monolithic plate with equivalent thicknesses, but its perforation resistance decreased with increasing number of layers [2]. The ballistic perforation resistance of double-layered armor-steel plates impacted by blunt and ogival projectiles were also examined, both experimentally and numerically [3]. The results shown that the ballistic limit was improved under the impact of flat-nose projectiles, compared to the monolithic counterpart of identical weight. In addition, the ballistic performance of multilayered and spaced mild steel target plates subjected to oblique impact of 7.62 armor piercing projectile was studied [4], but little difference among monolithic, multilayered and spaced targets was found. In general, when a monolithic target was replaced by a multilayered target, any likely improvement in ballistic performance was mainly attributed to the transition of failure mode from adiabatic shear plugging (dissipating less energy) to global plastic deformation and tensile tearing (dissipating much more energy) [5–8].

Due to excellent specific stiffness and strength, fiber reinforced plastic (FRP) composites have been increasingly employed in structural and armor applications [9–13]. However, thus far, while focus has been placed upon monolithic composite plates for ballistic applications, much less was devoted to evaluating multilayered laminates. A series of experiments were performed on double-layered aramid fiber composite targets [14] and it was found that that varying the thickness ratio of layers could lead to significant changes in ballistic resistance. More

* Corresponding authors.
E-mail addresses: hanbinghost@xjtu.edu.cn (B. Han), tjlu@nuaa.edu.cn (T.J. Lu).

https://doi.org/10.1016/j.ijimpeng.2021.104035
Received 20 January 2021; Received in revised form 26 September 2021; Accepted 29 September 2021
Available online 4 October 2021

recently, ultra-high molecular weight polyethylene (UHMWPE) fiber composites attracted much attention for their low density and superior mechanical properties, with cross-ply UHMWPE composite laminates exhibiting great advantages in defending ballistic threats of small-caliber projectiles [15–18]. It has been found that the ballistic impact behavior of UHMWPE was influenced by the rigidity of resin matrices [19] and the fabric folding configuration [20]. Further, an increase in ballistic limit (up to 10%) was achieved for double-layered targets with the areal density of 2~3 kg/m^2 [21]. However, physical mechanisms underlying the ballistic performance of multilayered UHMWPE cross-ply laminates remain elusive.

In the present work, the ballistic resistance of multilayered UHMMPE cross-ply laminates under the impact of blunt projectiles was investigated, both experimentally and numerically. Ballistic impacts were conducted on monolithic, double-layered and eight-layered laminates, respectively. In addition, flexible samples with 64 pre-preg layers were also tested under projectile impact. Dynamic deformation processes and failure modes were recorded and systematically compared. Further, the numerical simulation methodology was introduced and validated, which was then employed to explore the enhancement mechanisms of multi-layering.

2. Experiments

2.1. Material and specimen

Three types of cross-ply UHMWPE laminated plates were prepared for ballistic experiments, as shown in Fig. 1: Target A was an 8 mm monolithic laminated plate, Target B had two layers of 4 mm laminated plate, whereas Target C consisted of eight layers of 1 mm laminated plate. Thus, each target had a total thickness of 8 mm, with identical areal density of 7.68 kg/m^2 and in-plane dimensions of 300 mm × 300 mm. The UHMWPE layers in Targets B and C were simply stacked *without interface bonding*. In addition, flexible samples with 64 pre-preg layers (defined as Target D) were also prepared. Each layer of Target D consisted of two unidirectional plies in 0° and 90° directions, with a layer thickness of 0.15 mm. Since hot pressing was not performed on Target D, its total thickness was different from the other three target types, but its areal density remained the same as others.

The cross-ply UHMWPE laminate layers and prepregs were provided by the Beijing Tongyizhong New Material Technology Corporation, with commercial grade of HA792. Each pre-preg consisted of two unidirectional plies (0.075 mm thickness each) in 0° and 90° directions, with a total thickness of 0.15 mm. The UHMWPE fiber had a tensile strength above 3.8 GPa, a diameter of 17 μm and a volume fraction of 83%. Moreover, polyurethane resin was used as the matrix. Laminated targets were fabricated via stacking and hot pressing (under a temperature of 127 °C and a pressure of 20 MPa), with a ply lay-up angle of 90°.

Quasi-static uniaxial tensile tests were performed on the UHMWPE cross-ply laminate at a cross-head speed of 1 mm/min. Because of the high tensile strength and low shear strength for UHMWPE composites, the dog-bone samples suggested by Russell [22] were used to avoid shear/pull-out failure at the grips, as shown in Fig. 2(a). The strain was measured using a video extensometer by tracking the relative displacement of three points marked along the samples within the gauge length. Fig. 2(b) presented the measured stress and strain curves. The results showed that when the strain reached the peak of 2.75% where several plies near the surface delaminated and fractured, the stress continued to increase. After reaching the nominal tensile strength of 726 MPa, all fibers along the loading direction were fractured and serious delamination of the sample was observed. The tensile results demonstrated that due to the low interlaminar shear strength, the tensile load was not uniform in the cross-section. The same conclusion was drawn that the load from outer plys was not able to reach the core plys of UHMWPE laminates, resulting in the quite difficult measurement of the tensile material parameters [23,24]. Hence the measured nominal tensile strength should be lower than the actual value. However, the tensile properties of current material were similar to those of Dyneema® HB26 (i.e., the peak strength of 725 MPa and peak strain of 2.43%) [22].

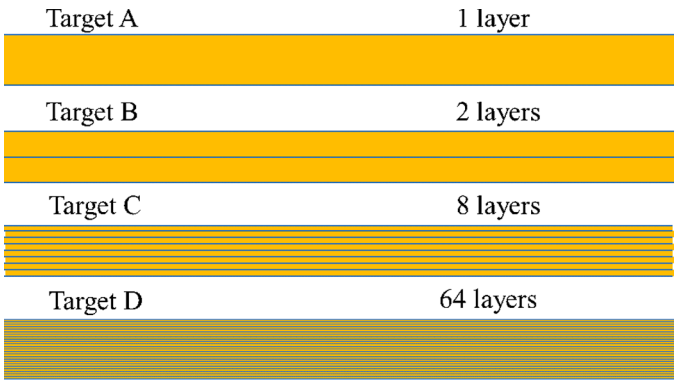

Fig. 1. Schematic of target configurations.

Quasi-static uniaxial compression was performed at a cross-head speed of 0.5 mm/min. Three square samples with the in-plane size of 50 mm and the thickness of 10 mm were waterjet cut from the laminated plate, and average results were reported in Fig. 3. The compression response was linear elastic and the Young's modulus was $E_c = 5.1$ GPa. At the peak compressive stress of $C_c = 1.74$ GPa, catastrophic failure occurred with significant acoustic emission.

2.2. Ballistic testing

Ballistic tests were performed using a two-stage light-gas gun, which was comprised of a gas chamber, a pump tube, a central breech assembly, a launch tube and a sample chamber, as shown schematically in Fig. 4(a). The length of the pump tube and launch tube were 2 m and 1.5 m, respectively. High purity nitrogen was compressed in the gas chamber and pump tube to accelerate the projectiles. Cylindrical projectiles, diameter 7.62 mm, length 20 mm, and mass 7.1 g, were fabricated from AISI4340 steel; Fig. 4(c). A sabot made of polyethylene (diameter 10 mm) was designed to drive the projectile out of the launch tube, which was attached behind the projectile during impact. However, because of the low weight (around 0.8 g) and strength (around 10 MPa) of sabot, its influence on the impact response of present target was negligible.

Details of target placement and velocity measurements were displayed in Fig. 4(b). Four clips were used to clamp the corners of each target to a fixture, thus little constraints had been applied in its in-plane direction. A high-speed camera (I-SPEED 510, IX) was employed to capture the dynamic deformation process and to measure the impact and residual velocities of the projectile. The exposure time was fixed at 2 μs and the inter-frame interval was 10 μs, with the time of initial impact defined as zero. The corresponded frame rate was 100000 Hz and the image resolution was 448 × 148 pix.

2.3. Experimental results

The ballistic results of impact velocity V_i, residual velocity V_r, and the energy absorption E were listed in Table 1 and plotted in Fig. 5(a). Here, the energy absorption E can be expressed by $E = E_i - E_r$, where E_i and E_r denotes the initial kinetic energy of projectile and residual kinetic energy of projectile, respectively. The energy absorption ratios $(E_i - E_r) / E_i$ were presented in Fig. 5(b). It was clear that an improvement in ballistic performance was achieved by multi-layering the target, and the enhancement effect was more pronounced as the number of layers was increased. In addition, the projectile with an initial velocity of 473 m/s could be fully stopped by Target B, but a large residual velocity of 223 m/s was left when impacted at 499 m/s, implying that the residual

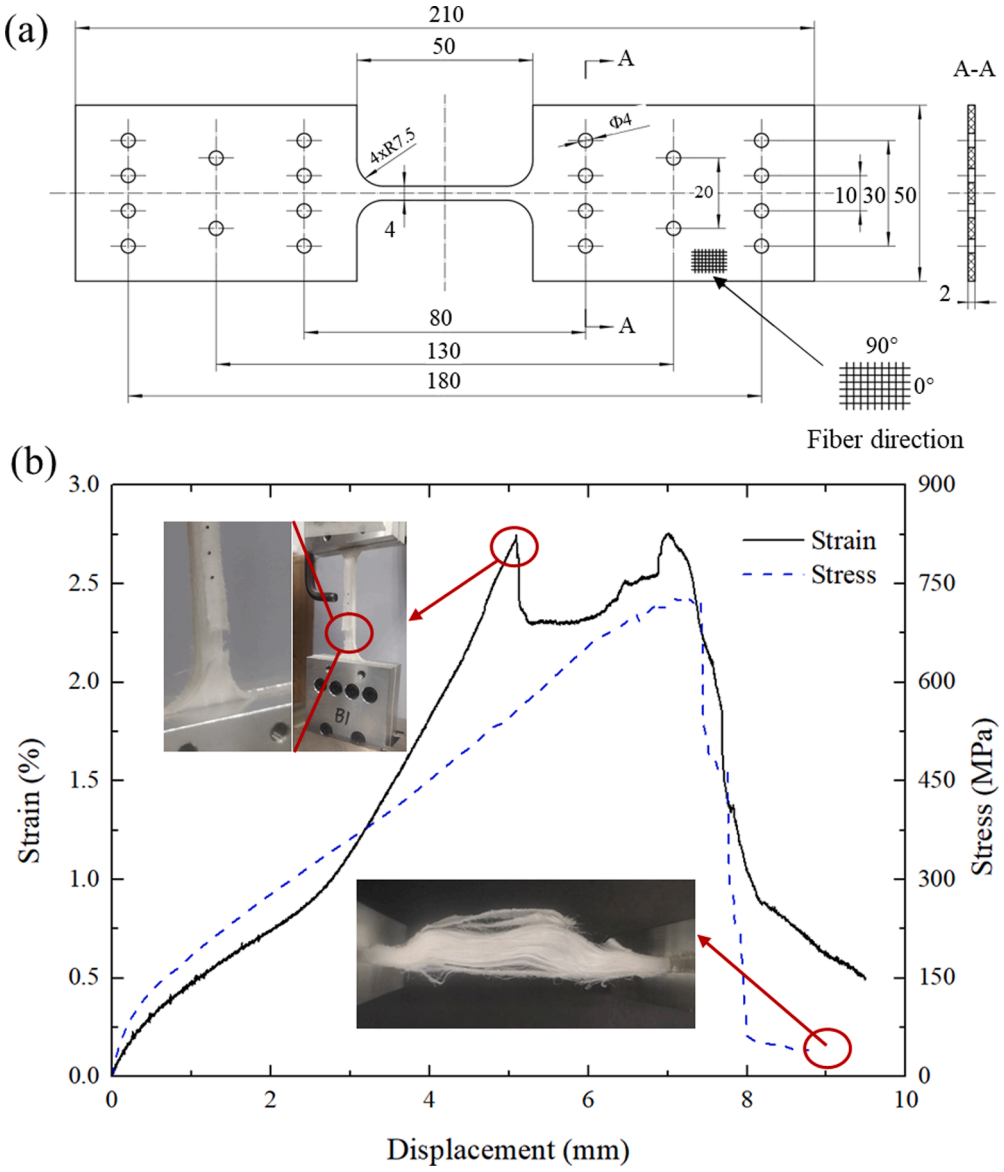

Fig. 2. (a) Geometry of the tensile sample and (b) the measured stress and strain curves.

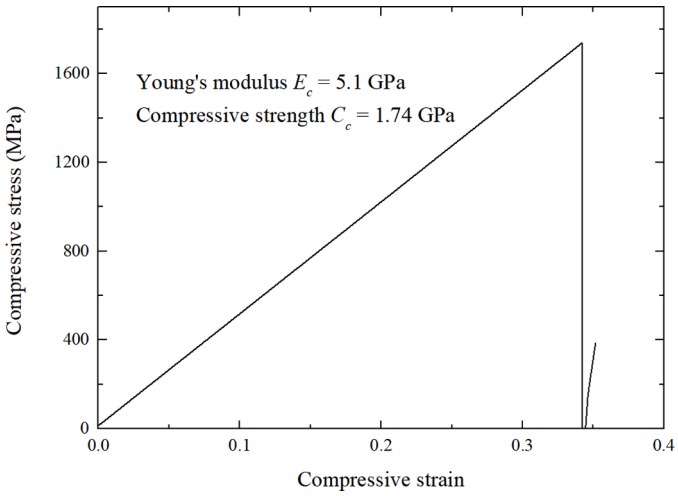

Fig. 3. The compressive stress versus strain curve of UHMWPE plate.

velocity increased sharply around the ballistic limit. Further, Target C was not perforated at 505 m/s, indicating the ballistic limit was indeed improved with multi-layering. In particular, the flexible Target D with 64 pre-preg layers (each 0.15 mm thick) exhibited superior resistance to projectile penetration and absorbed much more kinetic energy, as shown in Fig. 5(b). However, the dynamic response of this soft target was distinctly different from the other three target types, as shown in Fig. 6. When impacted at 522 m/s, although Target D was not perforated, the surviving layers suffered large bulging deformation, and the target was pulled out from the clips and flew away with projectile, the latter having a low residual velocity of 44 m/s. When the impact velocity was increased to 583 m/s, large bulge deformation still persisted in Target D, which was responsible for absorbing more impact energy. After the tests, all the flexible targets tested were found to fell off the fixture.

Fig. 7 displayed high-speed images of monolithic and multilayered targets impacted by projectile at velocity near ballistic limits. For the monolithic Target A (Fig. 7(a)), a bulge formed on its back face at 10 μs, growing continuously afterwards. At 300 μs, local delamination could be seen in the middle of the transverse boundary. As time proceeded further, the out-of-plane deflection no longer increased. After 400 μs, a

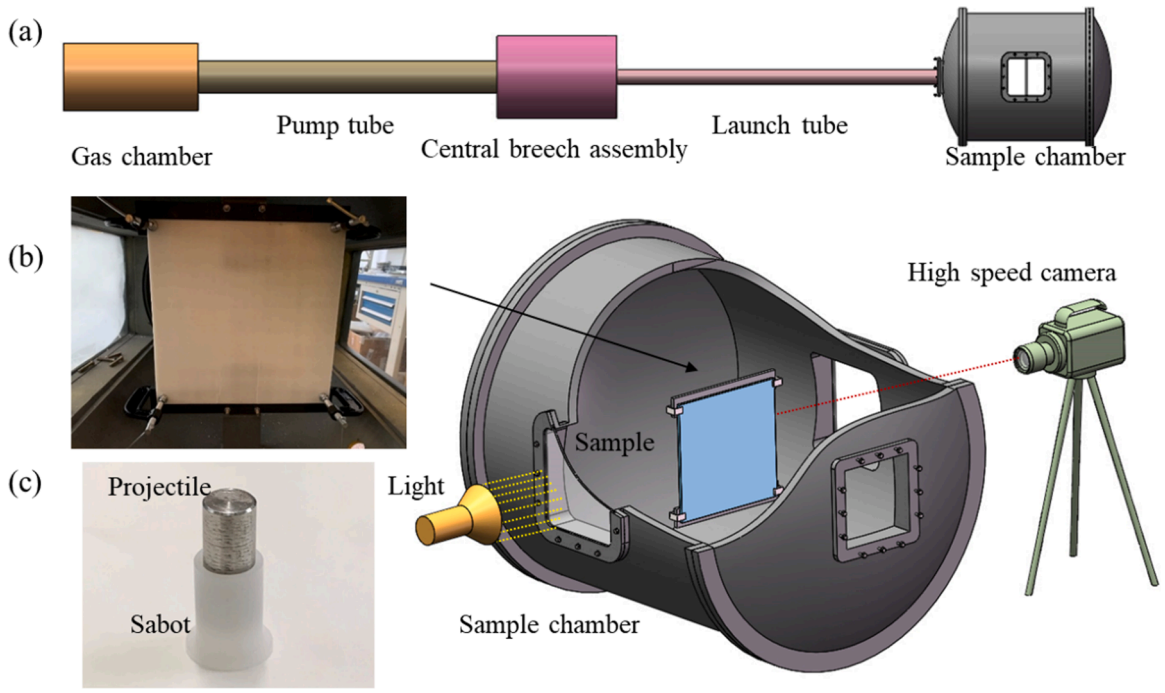

Fig. 4. (a) Schematic of ballistic testing setup, (b) arrangements of target placement and velocity measurements, and (c) photograph of projectile and sabot.

Table 1
Ballistic results of experiments and FE simulations.

Type	Impact velocity V_i (m/s)	Residual velocity V_r (m/s) Experiment	Simulation	Error (%)	Absorbed energy E (J)
A	446	0	0	0	706
	457	0	52	-	741
	513	267	271	1.5	681
	528	272	-	-	727
	522	288	288	0	673
	549	385	353	8.6	544
	580	470	-	-	410
	582	457	422	7.7	461
	600	500	472	9.4	390
B	473	0	0	0	794
	499	223	205	8.1	707
	527	326	270	17.2	609
	595	460	444	3.5	506
C	480	0	0	0	818
	505	0	0	0	905
	552	331	297	10.3	693
	559	279	310	11.1	833
	610	440	447	1.6	634
D	522	No Perforation	-	-	-
	583	339	-	-	799

rebounding motion of its back face was activated. As for the double-layered Target B (Fig. 7(b)), its out-of-plane deflection was larger than that of Target A, and the rebound was greatly diminished. Moreover, a kink-band was formed within the second layer in Target B. In comparison, the deflection of multilayered Target C was the largest and sustained up to 700 μs. Kink-bands similar to that found in Target B were observed within each of the two layers located at the back.

The deformation and failure modes of each target were examined after impact, and the results were presented in Fig. 8. Laminate folding could be detected at the front face of Target A, extending tangentially from its crater edge along fiber direction (Fig. 8(a)). However, such folding was barely detected in Targets B and C. From the back view, the permanent deflected profile seemed to be pyramidal in shape, with the ridges of the pyramid aligned along 0°/90° fiber orientations. Moreover, the *pull-in* phenomenon (*i.e.*, the laminate was pulled inwards from edges to central impact region) was obvious at the edges of the second layer in Target B and the back two layers in Target C, which corresponded to the above-mentioned kink-bands at the edges. In contrast, *pull-in* was barely observed in the monolithic Target A. From the cross-sectional view, severe delamination failures were observed in the back half of Target A, the second layer of Target B, and some penetrated layers of Target C. Overall, the permanent deflection was smallest in Target A, but largest in Target C.

The impact responses of Targets A, B and C under the impact velocities around 600 m/s were compared in Fig. 9, while their representative failure modes were compared in Fig. 10. It could be seen from Fig. 9 that the back face of Target A failed at 40 μs, whereas the back face failure was delayed to 48 μs for Target B. In comparison, around 50 μs, only slight damage was observed on the back of Target C. That is to say, as the number of layers was increased, the interaction between the projectile and the multilayered target lasted longer, resulting in smaller residual velocity. For all three target types, at sufficiently initial impact velocities, the projectile ejected with fractured fibers and exhibited little plastic deformation. After the perforation, the bulging of the target plate continued to grow, and the maximum deflection increased with increasing layer number. After the impact tests, an inspection of the back faces indicated that fiber fracture and ply splitting occurred in all targets, as shown in Fig. 10. Consistent with the lower velocity cases, delamination of plys occurred in all three targets, with Target C experiencing the largest permanent bulging deflection.

For impact velocities higher than the ballistic limit but less than the 600 m/s, the deformation and failure responses of Targets A, B and C were similar with the results shown in Figs. 9 and 10. As the impact velocity increased, the perforation appeared earlier, accompanying with the smaller deflection. From the comparison of the energy absorption of each experiment as listed in Table 1, it was revealed that there was a clear drop in energy absorption capability for impact velocity above the ballistic limit. The energy absorbed would be further decreased with the increase of impact velocity, which was caused by the earlier failure and smaller defection of the target.

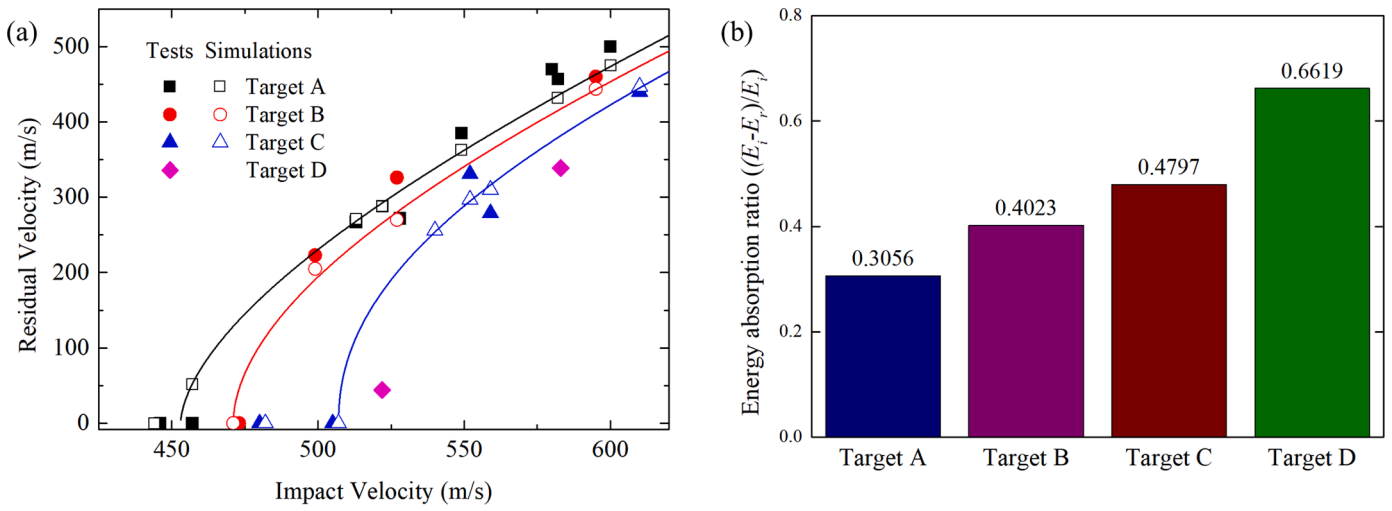

Fig. 5. (a) Residual velocity versus impact velocity of different target plates. (b) Ratios of absorbed energy to initial kinetic energy for different targets impacted at velocities around 600 m/s.

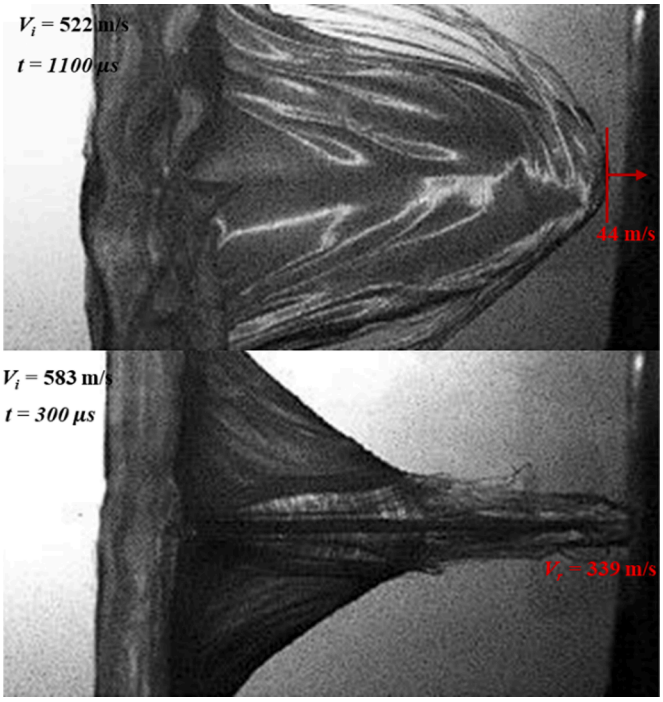

Fig. 6. Dynamic response of flexible Target D at selected initial impact velocities.

3. Simulations

3.1. Numerical modelling

The commercially available FE code LS-DYNA was utilized to numerically simulate the impact responses of the three hot-pressed target plates, *i.e.*, Targets A, B and C. Full three-dimensional model was built for each target, as shown schematically in Fig. 11. Generally, it was difficult to capture the delamination among laminate plies using continuum models. The sub-laminate model was proven to accurately simulate the ballistic deformation of UHMWPE laminates [25,26], and was adopted here. In current model, the laminated plate was modelled as a combination of sub-laminates, and each sub-laminate was considered as a homogeneous transversely isotropic plate representative of several cross-plies. Cohesive contacts were used to bond the adjacent sub-laminates, which also would possibly mimic the delamination failure of the interlaminar interface. Consequently, the delamination in cross-ply laminate as observed experimentally was simulated by the interface failure between sub-laminates.

For Target A, the 8 mm laminate was modeled as 16 bonded sub-laminates (each of 0.5 mm-thickness), as shown in Fig. 11(d), and a total of 15 cohesive contacts were defined. The failure criterion of cohesive contacts was given by:

$$\left(\frac{\sigma_n}{I_n}\right)^2 + \left(\frac{\sigma_s}{I_s}\right)^2 \geq 1 \tag{1}$$

where σ_n and σ_s were the normal and shear stresses, I_n and I_s were the normal and shear failure strengths. Prior to the interface failure, adjacent in-contacting sub-laminates were stuck together to transfer shear and tensile stresses. After the interface failed, the slippage and separation between sub-laminates were allowed. For Target B (2 layers), each layer of 4 mm-thickness was discretized as 8 bonded sub-laminates, with a general contact between the two 4 mm layers. As shown schematically in Fig. 11(e), 14 cohesive contacts and 1 general contact were defined in the model. The general contact was implemented to transfer compressive stress, without the stress transition of either interface shear or tension. Differently, 8 cohesive contacts and 7 general contacts were defined for Target C, which consisted of eight layers (each was constructed with two bonded sub-laminates), as shown schematically in Fig. 11(f).

In the sub-laminate model, each sub-laminate was considered as a homogeneous transversely isotropic plate representative of several cross-plies. However, the pre-preg layer of Target D consisted of only one 0° ply and one 90° ply, and the error would increase when equivalent to a homogeneous material. More importantly, Target D was not hot pressed and the flexibility was maintained, while the layers of Targets A, B and C were post-cured hard plates. The density of UHMWPE composite was changed by hot pressing because the resin would be squeezed out, and other mechanical properties might also be different. Due to the limitations of current sub-laminate method and material model, numerical simulation of the flexible Target D was not discussed here.

Both the projectile and laminated targets were meshed by element SOLID 164 based upon the Lagrangian formulation. A uniform element size of 0.5 mm was selected along the thickness direction, as depicted in Fig. 11(b). A finer in-plane mesh with 0.5 mm size was adopted for the central impact region (a 60 mm square region), and the element size at

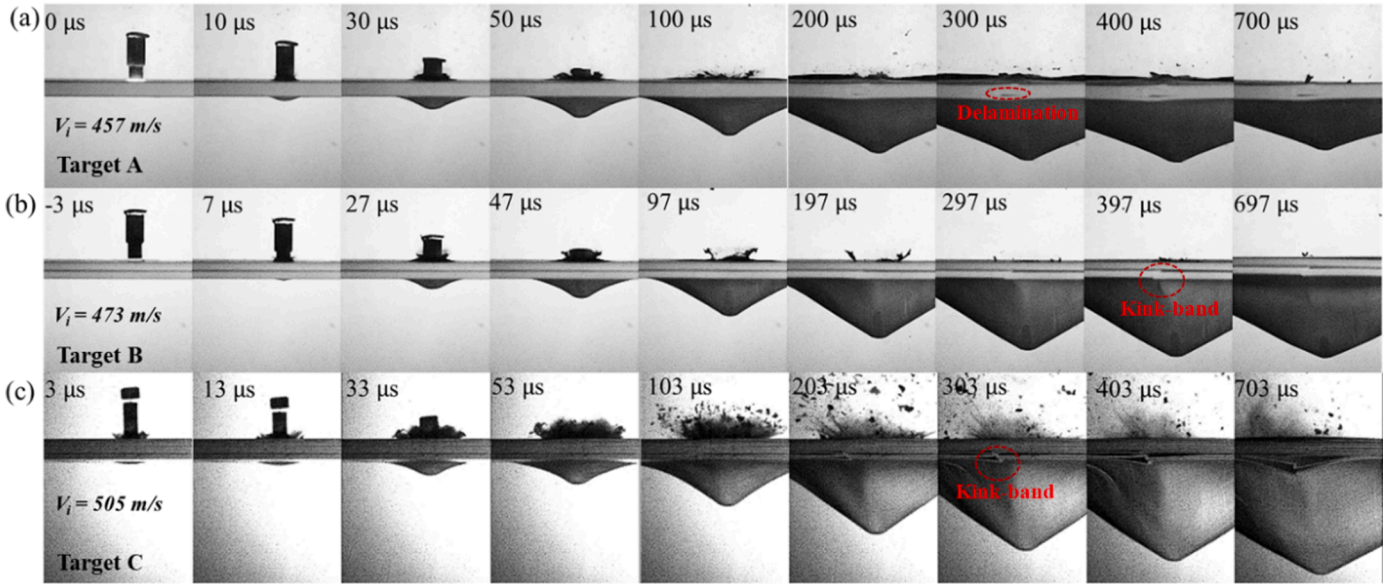

Fig. 7. High-speed image sequences of (a) Target A, (b) Target B, and (c) Target C at corresponding impact velocity just before complete penetration occurred.

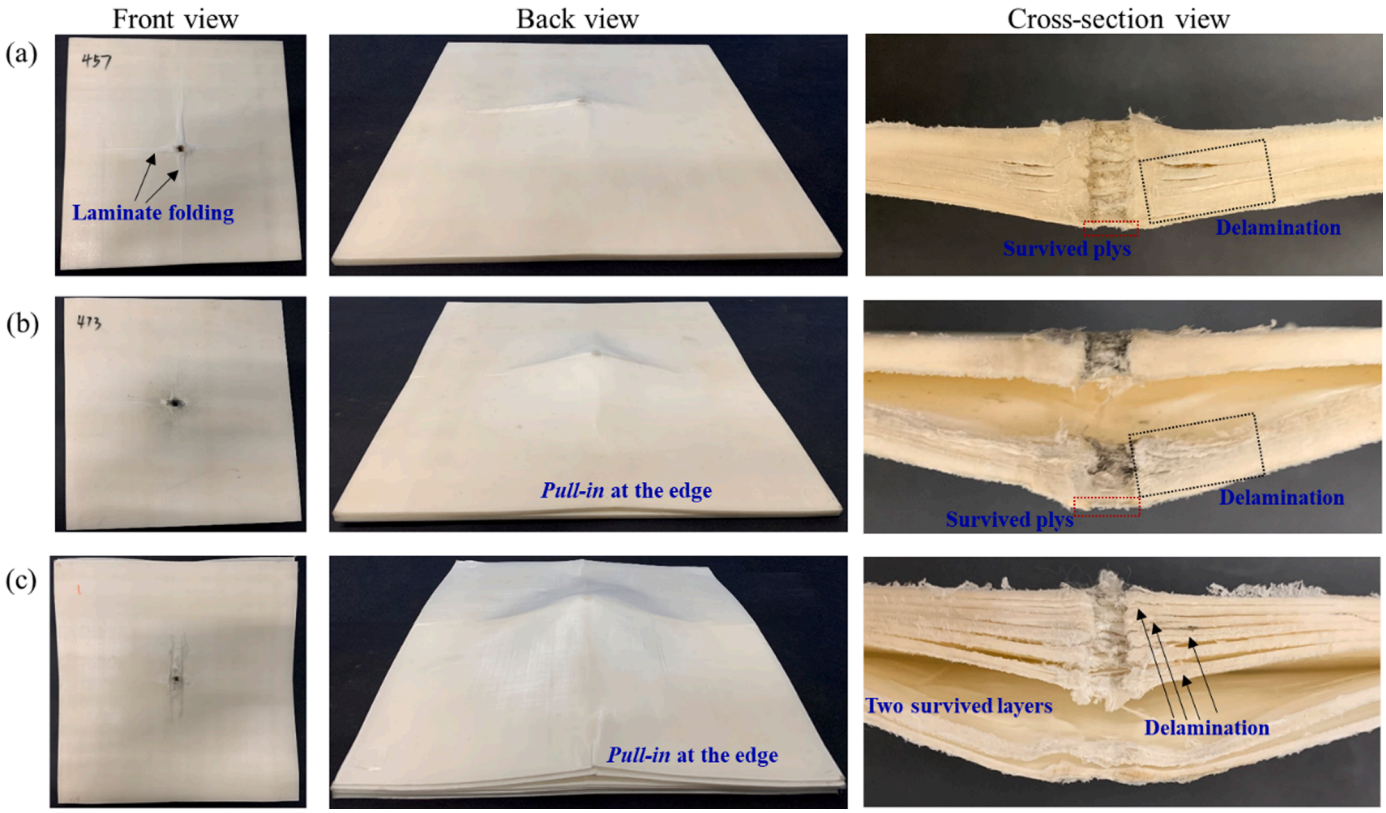

Fig. 8. Failure modes of (a) Target A impacted at 457 m/s, (b) Target B impacted at 473 m/s, and (c) Target C impacted at 505 m/s.

the boundary increased to 2 mm; Fig. 11(c). Besides, the projectile was meshed with an element size of 0.5 mm to match the mesh of target. In total, the element number of the final FE model was 610624. The convergence studies performed on the sub-laminate models [25–27] have confirmed that the current mesh style was able to achieve high numerical accuracy and low computational cost simultaneously.

Eroding-Surface-To-Surface contact options were set between the projectile and the laminated plate, with additional option of soft constraint formulation employed. Due to relatively weak constraint at the boundary, slippage at the clamp was observed in the experiments, and hence no boundary conditions were imposed on the targets in the present numerical models. Finally, to simulate the impact, an initial velocity was applied to the projectile.

3.2. *Material models and parameters*

The dynamic mechanical behavior of the present UHMWPE cross-ply laminate was modelled using a continuum composite constitutive model

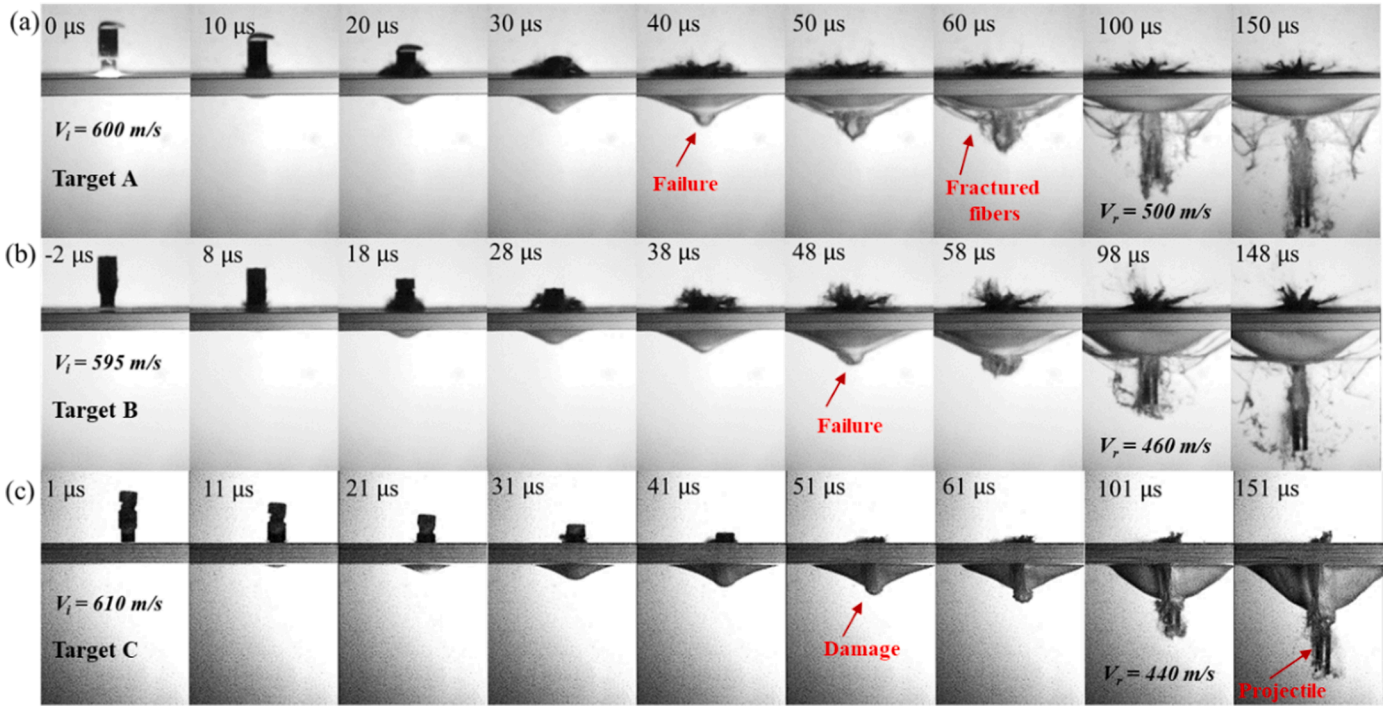

Fig. 9. High-speed image sequences of (a) Target A, (b) Target B, and (c) Target C impacted by projectile at velocities around 600 m/s.

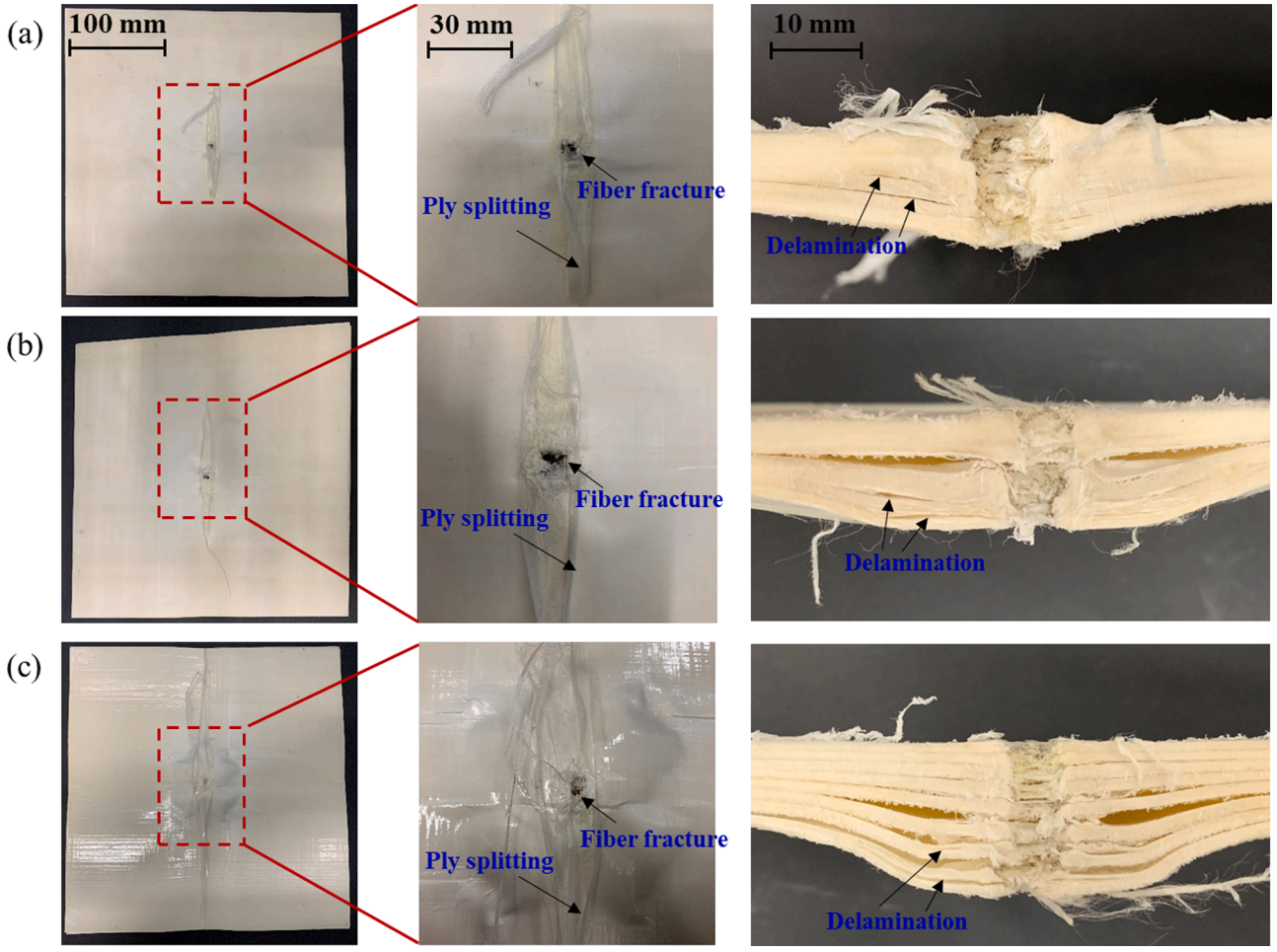

Fig. 10. Images of the back faces and cross-sections of (a) Target A impacted at 600 m/s, (b) Target B impacted at 595 m/s, and (c) Target C impacted at 610 m/s.

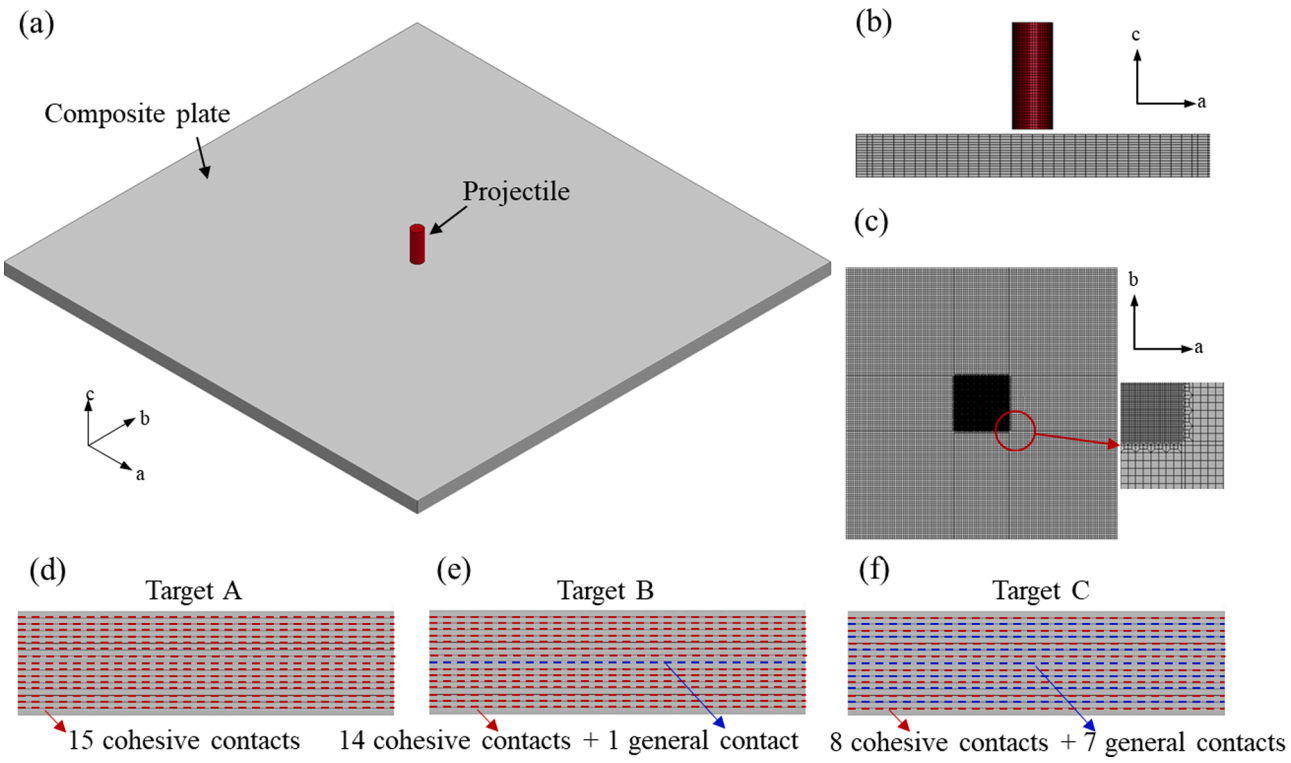

Fig. 11. (a) Three-dimensional model for UHMWPE laminated composite plate, with mesh details from (b) side view and (c) top view; schematic of modeling approach for (d) Target A, (e) Target B and (f) Target C.

with failure criteria, *i.e.*, material type #59 in LS-DYNA [27]. A linear elastic orthotropic stress and strain relation was implemented in this model. Due to the cross-ply layup adopted, identical material properties along 0° and 90° directions were assumed. The thermal independent methodology proposed by Nguyen et al. [25,28] have shown good correlation with the experimental results of 10 mm and 20 mm thick laminate, but failed to predict the penetration into a 36 mm target. Further, it was noted by Austin et al. [29] that in the case of 10 mm and 20 mm targets, thermal softening caused only 1% difference. Therefore, the thermal effect was only significant for thick laminates under impact velocity beyond 1000 m/s. In current experiments, the thickness of laminate was 8 mm and the velocity ranged from 400 m/s to 600 m/s, so the thermal softening was not implemented in the numerical model. Moreover, as tensile properties did not change at high strain rates [30], the strain rate dependency was neglected.

The equation of state was not included in the current material model. Thus, the hydrostatic pressure P was calculated by the constitutive model:

$$P = A_1\mu + A_2\varepsilon_a + A_3\varepsilon_b + A_4\varepsilon_c \tag{2}$$

where A_1, A_2, A_3, A_4 were material constants and can be specified independently from the stiffness matrix, and μ was the volumetric strain. In current orthotropic model, the relationship between pressure and volumetric strain was assumed to be linear, and the pressure was also related to deviatoric strain. In fact, the relationship between pressure and volumetric strain would become nonlinear for high pressure, and Nguyen et al. [25] incorporated the Mie-Gruneisen equation of state to describe the volumetric response. However, Hazzard et al. [26] have shown that the ballistic prediction was accurate at lower areal densities and impact velocities less than 600 m/s with the absence of equation of state. At higher areal densities and higher impact velocities, the ballistic limit from the simulation should be lower than experimental results.

Upon impact loading, the in-plane tensile strength and through-thickness compressive strength were defined to activate in-plane tensile failure and through-thickness compressive failure, as summarized in Table 2. In-plane and through-thickness shear strengths (S_{ab}, S_{ac}, S_{bc}) were set to infinite values due to the large shear strain at failure [31]. After failure, property degradation was performed within a short period by reducing the scaling factors of stiffness. The failed elements were eliminated when either or all of the following strains reached a critical value: tensile strain at 0.4 or compressive volumetric strain at 0.8. Element erosion strains were set to delete any highly distorted elements, which affect the time step and numerical stability without playing a further role in target interaction.

Table 3 listed the material parameters for UHMWPE composite that were used. The Young's modulus E_c and compressive strength C_c were measured from the compressive tests. Due to the difficulty of laminate tensile testing mentioned in Section 2.1, the tensile moduli of Dyneema® HB26 were used. It has been demonstrated that the intrinsic tensile strength of UHMWPE material should be used for numerical modeling [23], thus the values of in-plane tensile strengths (T_a and T_b) were obtained from single pre-preg tensile tests [24]. The Poisson's ratios and shear moduli were same with the Dyneema® HB26 [26]. The normal strength of cohesive contact I_n was taken from the largest measured value of through-thickness tensile strength under highly dynamic conditions [32], while the shear strength I_s was approximated by accounting for dynamic effects and the quasi-static interface shear

Table 2
Failure criterion of composite material model.

Failure mode	Criterion	
In-plane tensile failure	$\left(\frac{\sigma_a}{T_a}\right)^2 + \left(\frac{\tau_{ab}}{S_{ab}}\right)^2 + \left(\frac{\tau_{ac}}{S_{ac}}\right)^2 \geq 1$	(1)
	$\left(\frac{\sigma_b}{T_b}\right)^2 + \left(\frac{\tau_{ab}}{S_{ab}}\right)^2 + \left(\frac{\tau_{bc}}{S_{bc}}\right)^2 \geq 1$	(2)
Through-thickness compressive failure	$\left(\frac{\sigma_c}{S_{ac}+S_{bc}}\right)^2 + \left[\left(\frac{C_c}{S_{ac}+S_{bc}}\right)^2 - 1\right]\frac{\sigma_c}{\lvert C_c\rvert} + \left(\frac{\tau_{ac}}{S_{ac}}\right)^2 + \left(\frac{\tau_{bc}}{S_{bc}}\right)^2 \geq 1$	(3)

Table 3
Material parameters used in the FE simulations.

Parameters of *UHMWPE*	Value	Ref.	Parameters of *AISI 4340 steel*	Value	Ref.
Young's modulus, E_a (GPa)	34.257	[26]	Shear modulus, G (GPa)	77	[33]
Young's modulus, E_b (GPa)	34.257	[26]	Bulk modulus, K (GPa)	159	[33]
Young's modulus, E_c (GPa)	5.1	*	Static yield strength, A (GPa)	0.785	[33]
Poisson's ratio, ν_{ba}	0	[26]	Hardening constant, B (GPa)	0.510	[33]
Poisson's ratio, ν_{ca}	0.013	[26]	Strain hardening exponent, n	0.260	[33]
Poisson's ratio, ν_{cb}	0.013	[26]	Strain rate constant, C	0.014	[33]
Shear modulus, G_{ab} (GPa)	0.1738	[26]	Thermal softening exponent, m	1.03	[33]
Shear modulus, G_{ca} (GPa)	0.5478	[26]	Reference strain rate, $\dot{\varepsilon}_0$ (s^{-1})	1.0	[33]
Shear modulus, G_{cb} (GPa)	0.5478	[26]	Melting temperature, t_m (K)	1793	[33]
Tensile strength, T_a (GPa)	1.25	[24]	Damage constant, d_1	0.05	[33]
Tensile strength, T_b (GPa)	1.25	[24]	Damage constant, d_2	3.44	[33]
Compressive strength, C_c (GPa)	1.74	*	Damage constant, d_3	-2.12	[33]
Normal strength, I_n (MPa)	60	[32]	Damage constant, d_4	0.002	[33]
Shear strength, I_s (MPa)	80	[16]	Damage constant, d_5	0.61	[33]

* Parameters measured from uniaxial compressive tests.

strength [16]. As for the AISI 4340 steel projectile, the Johnson-Cook constitutive and failure models were employed, and relevant parameters taken from [33] were also listed in Table 3.

3.3. Validation

Numerical results for Targets A, B and C were presented in Fig. 5(a), while quantitative comparison with experimental results was given in Table 1. Good agreement was achieved for the prediction of residual velocity. Further, the experimentally observed bulge evolution process was well mimicked by the present FE simulations, as shown in Fig. 12(a). The numerically predicted back face deflections were plotted in Fig. 12 (b) as functions of impact time, and compared with experimental measurements. The numerical model successfully replicated the tendency that the deflection of the back face increased with increasing layer number. However, the deflection was somewhat underestimated by FE predictions for all three targets, mainly attributed to two reasons: (1) interface failure (*i.e.*, delamination) in the FE model was only allowed among sub-laminates with a thickness of 0.5 mm, while it could occur in individual plies of only 0.075 mm thickness for the actual cross-ply laminate; (2) some of the key material properties, e.g., elastic and shear moduli of UHMWPE fibers, may be degraded by thermal loads during impact, which was not considered by the numerical model. Nonetheless, overall, the predictions of the present numerical simulations were considered reasonable.

4. Discussions

4.1. Effect of membrane stretching

The history of numerically computed tensile stress along fiber direction at the central point of the back face was presented in Fig. 13 for Targets A, B and C. When the initial velocity of 400 m/s (Fig. 13(a)) was relatively low, the three targets were all not perforated. The dynamic response could be broadly divided into local bending and membrane stretching. Local bending occurred within the first 10 μs, leading to a sharp increase in back face tensile stress along the fiber direction. Subsequently, as the bulging grew, the deformation mode changed from local bending to membrane stretching, with debonding or delamination emerging around the impact region. The present numerical results also indicated that the average membrane tensile stress was largest in Target A, but smallest in Target C.

As shown in Fig. 13(b), when the impact velocity was increased to 500 m/s, the peak tensile stress at the stage of local bending was correspondingly increased. At 40 μs, a large portion of Target A ruptured and was penetrated by the projectile, leaving the last undamaged part having only a thickness of 3 mm. At the time around 70 μs, the tensile stress on the back face reached the failure strength, resulting in perforation. Such tensile failure, due to direct contact of the projectile with the last few intact sub-laminates, was delayed in Target B and was prohibited in Target C. At 40 μs, the undamaged laminate in Target C had a thickness of 4 mm. Thus, more resistance against projectile penetration was provided by Target C and the projectile velocity was significantly reduced, with no perforation of the back face.

As the impact velocity was further increased to 600 m/s, all targets were perforated, with the responses of Target A and C highlighted in Fig. 14. The rupture of the back face in Target A occurred early (around 35 μs), since the tensile stress on the back face fleetly reached the tensile strength. However, less damage could be found for Target C until 40 μs, consistent with the experimental observation.

The experimentally observed *pull-in* phenomenon at the edges was replicated in simulations, as shown in Fig. 15. For Target A impacted at

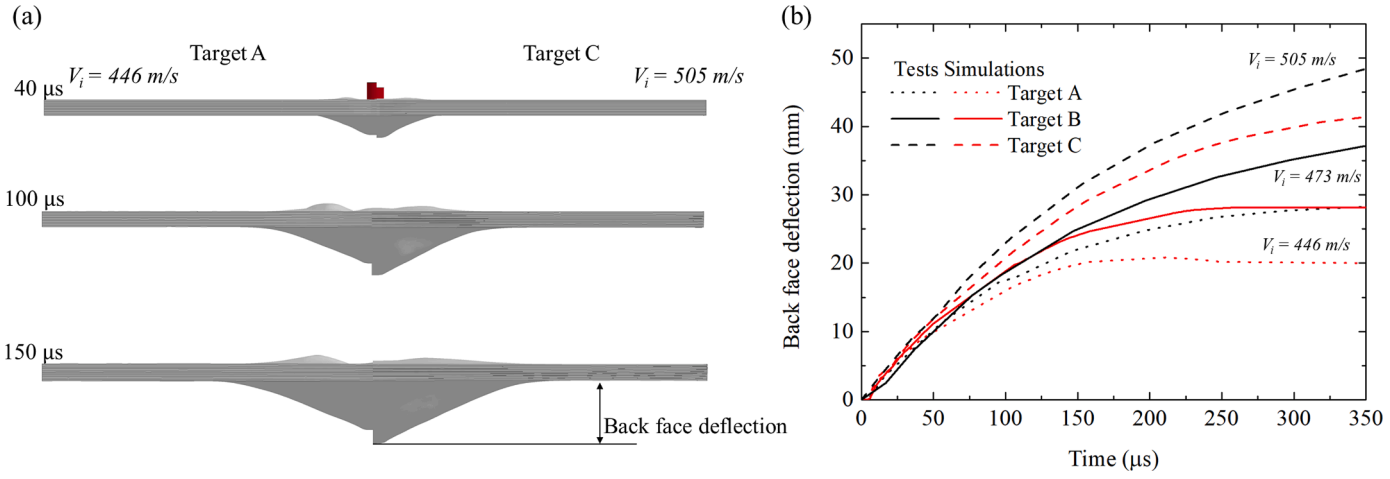

Fig. 12. (a) Numerically simulated dynamic deformation responses and (b) comparison of predicted back face deflections with experimental measurements.

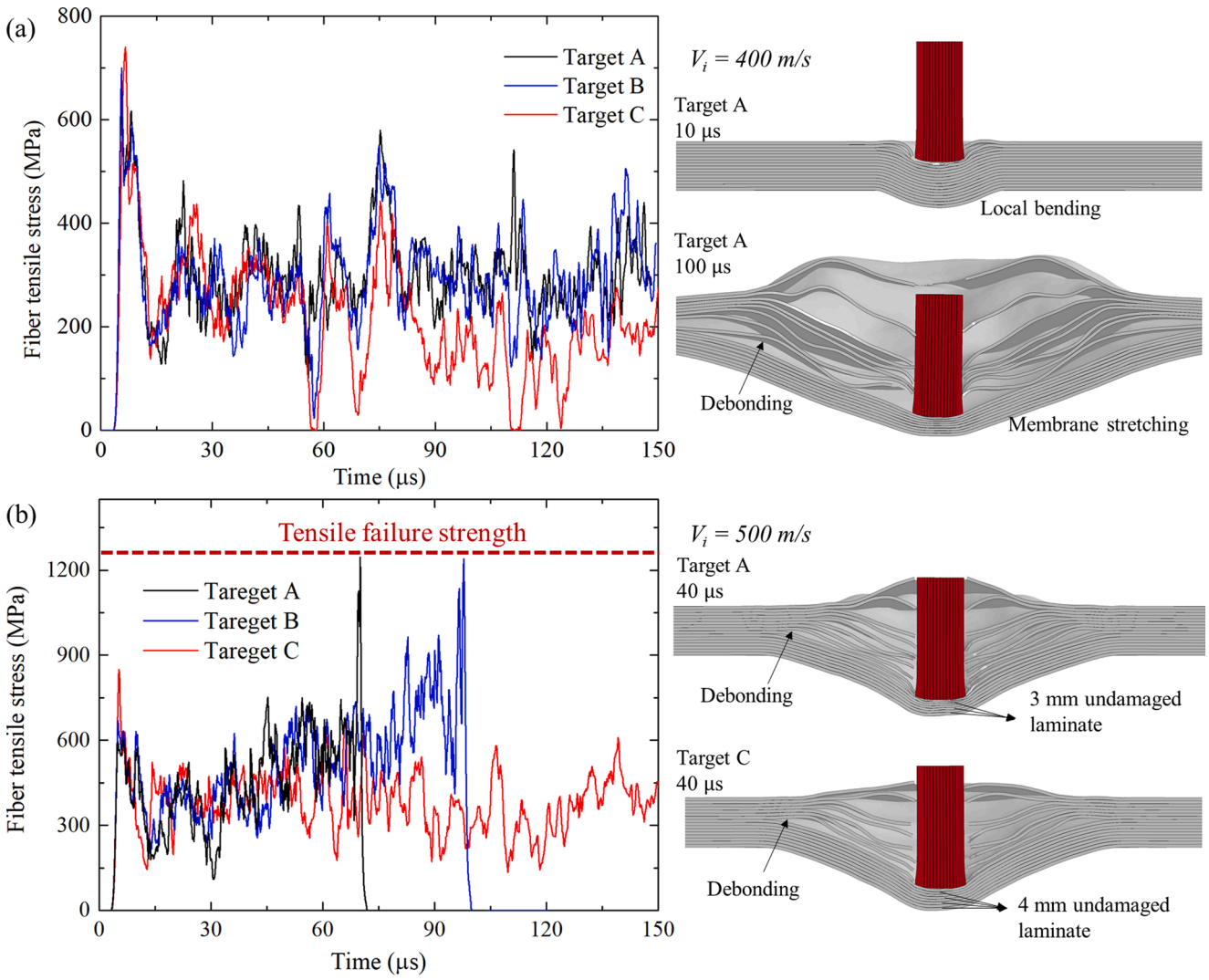

Fig. 13. Numerically calculated histories of fiber tensile stress at the center of back face at impact velocity of (a) 400 m/s and (b) 500 m/s for Targets A, B and C, with selected failure modes also presented.

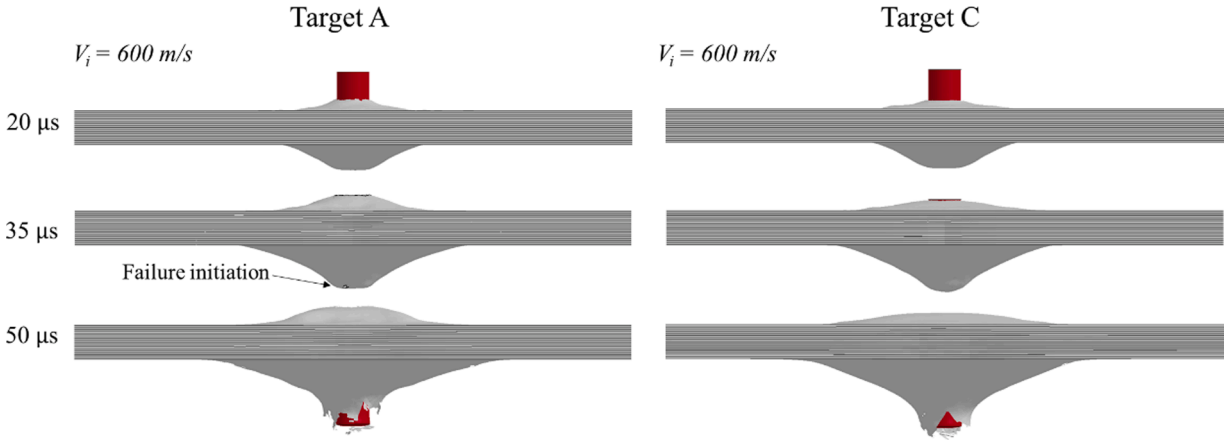

Fig. 14. Penetration responses of Target A and C impacted by projectile at 600 m/s.

the velocity near ballistic limit, although a large portion of the laminate was penetrated by the projectile, the pull-in length at all the edges was almost the same throughout its thickness, due to strong restrictions at the well-bonded interfaces of the sub-laminates. In the double-layered Target B, however, this pull-in effect in the second layer was more significant than that in the first layer. Further, for Target C which was discretized to 8 layers, the pull-in length of each layer increased in order from the front to the back. In particular, the pull-in effect in the last layer

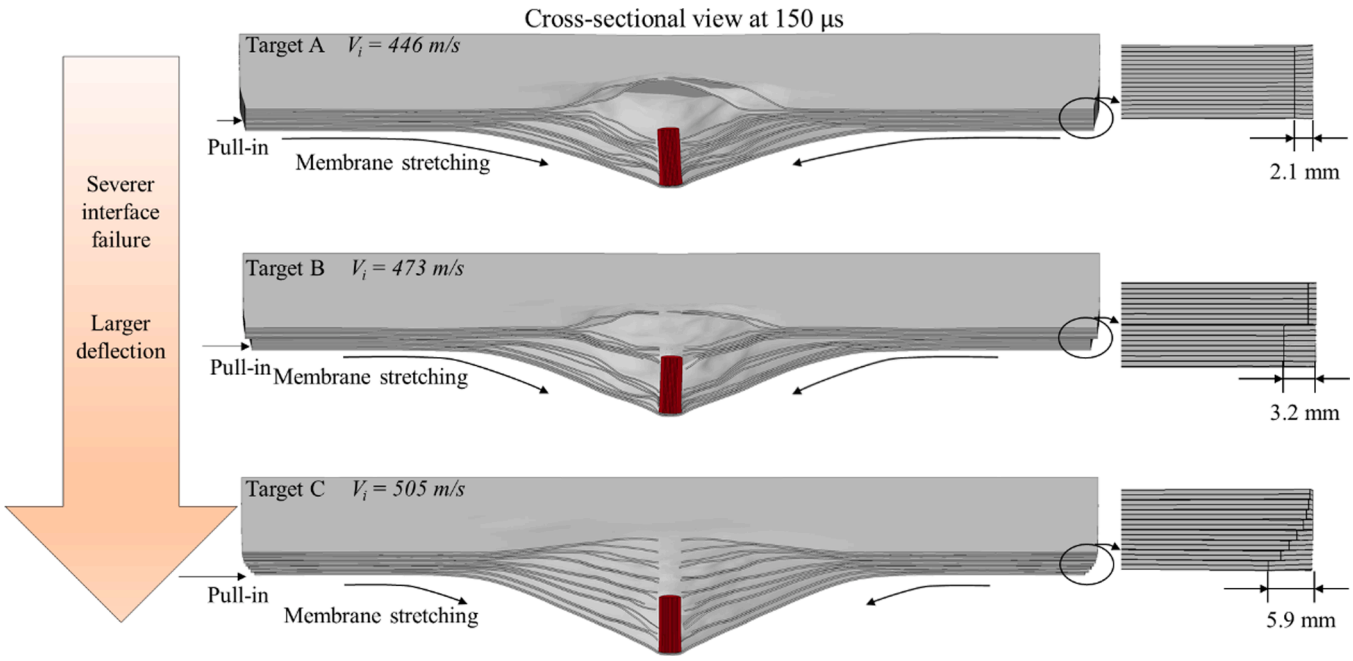

Fig. 15. Pull-in effects of Targets A, B and C impacted at velocities near respective ballistic limits.

was the most notable, corresponding to the largest deflection of the rear layer that absorbed much more energy. Meanwhile, the lack of restrictions at the interfaces and the pull-in effect were responsible for the lower membrane stress sustained by the back face of Target C, which prevented the penetration of the last few layers.

4.2. Penetration mechanisms

According to the experimental results shown in Section 2.3 and the observations of existing literatures [12,16], the UHMWPE laminates failed in a progressive manner, and the penetration process could be divided into two stages, as shown in Fig. 16(a): (i) the initial penetration was accompanied by local deformation and failure, and (ii) then the membrane stretching was activated and severe delamination occurred. Once the impact occurred, a compressive shock wave would be generated below the projectile and propagate to the back face. The huge contact pressure between projectile and laminate after initial impact was responsible for the local deformation and failure beneath the projectile. Hazzard et al. [26] and Zhang et al. [27] have numerically found that the contact pressure between projectile and laminate would be significantly reduced by tensile relief wave (C_h) reflected from the rear free face, which might be the mechanism the change in failure mode from local failure to membrane stretching.

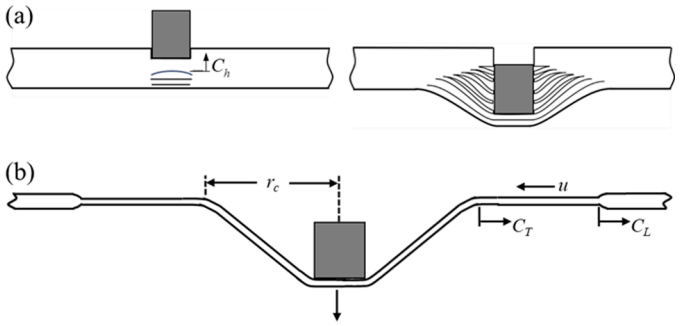

Fig. 16. Schematic illustrations of the failure of the UHMWPE laminates: (a) the progressive failure of UHMWPE composite and (b) the wave propagation and deformation during membrane stretching.

A schematic illustration of membrane deformation and wave propagation was shown in Fig. 16(b). When the contact pressure exerted by projectile was insufficient to induce local failure of fibers, the intact fraction of laminate continued to deflect, with membrane stretching activated. Considering a membrane impacted by the projectile, longitudinal and transverse waves would be generated and propagate along the fibers. The longitudinal wave C_L stretched fibers in the plane and led to the inflow of the membrane with velocity of u, while the transverse wave C_T resulted in the out-of-plane displacement and changed the inflow velocity. The large deflection of the cone without failure was allowed by the inflowing of the intact sublayers into the projectile region, rather than the membrane strain. The membrane strain during deformation process was evaluated by current numerical simulation, and the results shown that the membrane strain under the projectile was around 3.5% when impacted near the ballistic limit. O'Masta et al. [34] measured the extension of UMMWPE laminates and found the elongation of fibers did not exceed 3% throughout the deformation history. A membrane model for the ballistic impact was developed by Phoenix and Porwal [35], and they indicated that only 20% of the large deflection was due to the membrane strain and the other 80% came from the inflow.

The current experimental and numerical results both showed that the multilayered targets corresponded to larger deflection. For the multilayered plates, stresses across the section cannot be supported, and stress gradient arising from bending and shearing would be relieved, so the failure at the rear would be delayed. Similarly, for double-layered metal target, Dey et al. [3] found that the shear plugging occurred in the first plate was prevented in the second. Thus, global deformation and membrane stretching were able to take place. Moreover, the pull-in effect presented in Figs. 8 and 15 was caused by the inflow of membrane, and initiated once the longitudinal wave reflected at the edge. The larger pull-in length corresponded to more material inflowing into the cone (see Fig. 15), which corresponded to a larger deflection.

To further explore the enhancement mechanisms of multilayered target, the computed projectile velocity as a function of time for different targets at an impact velocity of 500 m/s was plotted in Fig. 17 (a). It could be drawn that the discrepancy between Target A and C even occurred in the early stage of penetration. Fig. 17(b) compared the absorbed energy of targets in terms of the deformation (*i.e.*, internal

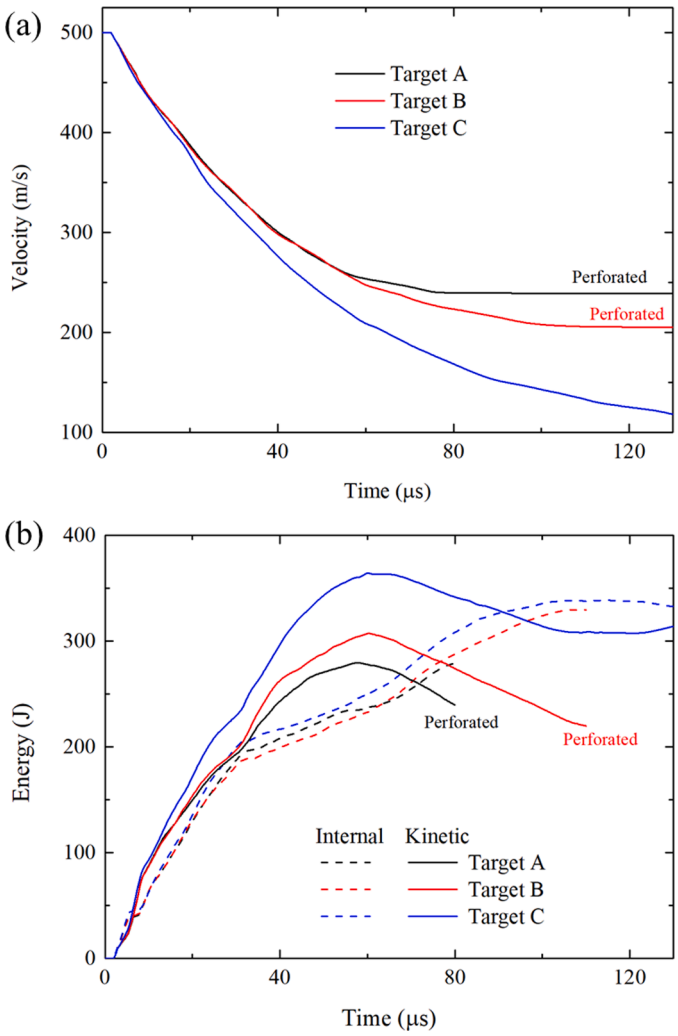

Fig. 17. (a) The projectile velocity histories and (b) energy absorption of different targets at impact velocity of 500 m/s.

energy) and the movement (*i.e.*, kinetic energy). The difference of the internal energy for different targets seemed to be little, while the kinetic energy was increased as the layer increased. It was noted the kinetic energy of three targets all reached the maximum around 60 μs, which was equivalent to twice of the time for the longitudinal wave travelling from the center to the edge. The results presented in Figs. 7, 12(b) and 17 (b) implied that the inflow velocity of the membrane for multilayered targets was relatively higher. This higher inflow velocity was induced by the lack of restriction between sublayers, and was responsible for the larger pull-in length to sustain larger deflection without the tensile failure.

Recently, it has been reported by Karthikeyan et al. [16], Wang et al. [19] and Cline et al. [36] that the UHWMPE laminate with weaker matrix and lower shear strength performed much better in perforation resistance and energy absorption. Compared with the monolithic UHMWPE laminate, the multilayered target had no matrix connection in the interfaces of adjacent sublayers and could not bear the interlaminar shear. Therefore, the results of present study were consistent with those reported in the literatures.

5. Concluding remarks

The ballistic performance of multilayered cross-ply UHMWPE laminated plate was investigated. Targets with different number of layers but the same areal density were tested and simulated. The main conclusions drawn from the study were summarized as follows:

1. The penetration resistance of UHMWPE laminated plate could be improved by layering the target, and the enhancement was more pronounced as the number of layers was increased.

2. The deflection profiles of monolithic and multilayered UHMWPE targets were pyramid-shaped. Further, fiber fracture, ply splitting and delamination failure occurred in all targets. However, a larger back face deflection could be observed in the multilayered target, with the failure time of its back face delayed.

3. The superior ballistic resistance of the multilayered target was attributed to the lack of restriction between sublayers. As a result, more material could flow into the cone, and the fiber tensile stress on the back face could be lower, thereby withstanding larger deflection without the tensile failure.

CRediT authorship contribution statement

Rui Zhang: Methodology, Conceptualization, Writing – original draft. **Bin Han:** Writing – review & editing, Resources. **Jun-Yang Zhong:** . **Lu-Sheng Qiang:** Visualization, Data curation. **Chang-Ye Ni:** . **Qi Zhang:** . **Qian-Cheng Zhang:** . **Bin-Chao Li:** . **Tian Jian Lu:** Writing – review & editing, Supervision.

Declaration of Competing Interest

The authors declare that they have no known competing financial interests or personal relationships that could have appeared to influence the work reported in this paper.

Acknowledgment

The authors gratefully acknowledge the financial support by the National Natural Science Foundation of China (11802221, 11972185, 11902148, 12002156 and 12032010), the Open Fund of the State Key Laboratory of Mechanics and Control of Mechanical Structures (MCMS-I-0219K01 and MCMS-E-0219K02), the Natural Science Fund Project in Jiangsu Province of China (BK20190392), and the Fundamental Research Funds for the Central Universities (grant numbers xtr012019004 and zrzd2017027).

References

[1] Teng X, Dey S, Børvik T, Wierzbicki T. Protection performance of double-layered metal shields against projectile impact. J Mech Mater Struct 2007;2:1309–29.
[2] Gupta NK, Iqbal MA, Sekhon GS. Effect of projectile nose shape, impact velocity and target thickness on the deformation behavior of layered plates. Int J Impact Eng 2008;35:37–60.
[3] Dey S, Børvik T, Teng X, Wierzbicki T, Hopperstad OS. On the ballistic resistance of double-layered steel plates: an experimental and numerical investigation. Int J Solids Struct 2007;44:6701–23.
[4] Iqbal MA, Senthil K, Madhu V, Gupta NK. Oblique impact on single, layered and spaced mild steel targets by 7.62 AP projectiles. Int J Impact Eng 2017;110:26–38.
[5] Alavi Nia A, Hoseini GR. Experimental study of perforation of multi-layered targets by hemispherical-nosed projectiles. Mater Des 2011;32:1057–65.
[6] Holmen JK, Solberg JK, Hopperstad OS, Børvik T. Ballistic impact of layered and case-hardened steel plates. Int J Impact Eng 2017;110:4–14.
[7] Liu J, Long Y, Ji C, Liu Q, Zhong M, Zhou Y. Influence of layer number and air gap on the ballistic performance of multi-layered targets subjected to high velocity impact by copper EFP. Int J Impact Eng 2018;112:52–65.
[8] Wei Z, Yunfei D, Sheng CZ, Gang W. Experimental investigation on the ballistic performance of monolithic and layered metal plates subjected to impact by blunt rigid projectiles. Int J Impact Eng 2012;49:115–29.
[9] Santhanakrishnan Balakrishnan V, Hart-Rawung T, Buhl J, Seidlitz H, Bambach M. Impact and damage behaviour of FRP-metal hybrid laminates made by the reinforcement of glass fibers on 22MnB5 metal surface. Compos Sci Technol 2020;187.
[10] Zhang R, Han B, Lu TJ. Confinement effects on compressive and ballistic performance of ceramics: a review. Int Mater Rev 2021;66(5):287–312.
[11] Mousavi MV, Khoramishad H. Investigation of energy absorption in hybridized fiber-reinforced polymer composites under high-velocity impact loading. Int J Impact Eng 2020;146:103692.

[12] Nguyen LH, Ryan S, Cimpoeru SJ, Mouritz AP, Orifici AC. The effect of target thickness on the ballistic performance of ultra high molecular weight polyethylene composite. Int J Impact Eng 2015;75:174–83.
[13] Quan C, Han B, Hou Z, Zhang Q, Tian X, Lu TJ. 3D printed continuous fiber reinforced composite auxetic honeycomb structures. Compos Part B 2020;187:107858.
[14] Wielewski E, Birkbeck A, Thomson R. Ballistic resistance of spaced multi-layer plate structures: experiments on fibre reinforced plastic targets and an analytical framework for calculating the ballistic limit. Mater Des 2013;50:737–41.
[15] Reddy TS, Reddy PRS, Madhu V. Response of E-glass/epoxy and Dyneema ® composite laminates subjected to low and high velocity impact. Proc Eng 2017;173:278–85.
[16] Karthikeyan K, Russell BP, Fleck NA, Wadley HNG, Deshpande VS. The effect of shear strength on the ballistic response of laminated composite plates. Eur J Mech A Solids 2013;42:35–53.
[17] Nguyen LH, Ryan S, Cimpoeru SJ, Mouritz AP, Orifici AC. The efficiency of ultra-high molecular weight polyethylene composite against fragment impact. Exp Mech 2015;56:595–605.
[18] Zhao ZN, Han B, Zhang R, Zhang Q, Zhang QC, Ni CY, Lu TJ. Enhancement of UHMWPE encapsulation on the ballistic performance of bi-layer mosaic armors. Compos Part B 2021;221:109023.
[19] Wang H, Hazell PJ, Shankar K, Morozov EV, Escobedo JP. Impact behaviour of Dyneema® fabric-reinforced composites with different resin matrices. Polym Test 2017;61:17–26.
[20] Wang H, Hazell PJ, Shankar K, Morozov EV, Escobedo JP, Wang C. Effects of fabric folding and thickness on the impact behaviour of multi-ply UHMWPE woven fabrics. J Mater Sci 2017;52:13977–91.
[21] Karthikeyan K, Russell BP. Polyethylene ballistic laminates: failure mechanics and interface effect. Mater Des 2014;63:115–25.
[22] Russell BP, Karthikeyan K, Deshpande VS, Fleck NA. The high strain rate response of ultra high molecular-weight polyethylene: from fibre to laminate. Int J Impact Eng 2013;60:1–9.
[23] Iannucci L, Del Rosso S, Curtis PT, Pope DJ, Duke PW. Understanding the thickness effect on the tensile strength property of Dyneema® HB26 laminates. Materials 2018;11(8):1431.
[24] Heisserer U, Werff Hvd. Strength matters: which strength of DYNEEMA® fiber composites to use in hydrocode models?-A discussion. In: 29th International symposium on ballistics; 2016.
[25] Nguyen LH, Lässig TR, Ryan S, Riedel W, Mouritz AP, Orifici AC. A methodology for hydrocode analysis of ultra-high molecular weight polyethylene composite under ballistic impact. Compos Part A 2016;84:224–35.
[26] Hazzard MK, Trask RS, Heisserer U, Van Der Kamp M, Hallett SR. Finite element modelling of Dyneema® composites: from quasi-static rates to ballistic impact. Compos Part A 2018;115:31–45.
[27] Zhang R, Qiang LS, Han B, Zhao ZY, Zhang QC, Ni CY, et al. Ballistic performance of UHMWPE laminated plates and UHMWPE encapsulated aluminum structures: numerical simulation. Compos Struct 2020;252:112686.
[28] Nguyen L. The ballistic performance of thick ultra high molecular weight polyethylene composite. RMIT University; 2015.
[29] Austin S, Brown AD, Escobedo JP, Wang H, Kleine H, Hazell PJ. The high-velocity impact of Dyneema® and Spectra® laminates: implementation of a simple thermal softening model. Proc Eng 2017;204:51–8.
[30] Wang H, Hazell PJ, Shankar K, Morozov EV, Jovanoski Z, Brown AD, Li Z, Escobedo-Diaz JP. Tensile properties of ultra-high-molecular-weight polyethylene single yarns at different strain rates. J Compos Mater 2019;54:1453–66.
[31] Lässig T, Nguyen L, May M, Riedel W, Heisserer U, van der Werff H, Hiermaier S. A non-linear orthotropic hydrocode model for ultra-high molecular weight polyethylene in impact simulations. Int J Impact Eng 2015;75:110–22.
[32] Lässig T, Bagusat F, Pfändler S, Gulde M, Heunoske D, Osterholz J, Stein W, Nahme H, May M. Investigations on the spall and delamination behavior of UHMWPE composites. Compos Struct 2017;182:590–7.
[33] Zhang R, Han B, Li L, Zhao ZN, Zhang Q, Zhang QC, Ni CY, Lu TJ. Influence of prestress on ballistic performance of bi-layer ceramic composite armors: experiments and simulations. Compos Struct 2019;227:111258.
[34] O'Masta MR, Deshpande VS, Wadley HNG. Mechanisms of projectile penetration in Dyneema® encapsulated aluminum structures. Int J Impact Eng 2014;74:16–35.
[35] Leigh Phoenix S, Porwal PK. A new membrane model for the ballistic impact response and V50 performance of multi-ply fibrous systems. Int J Solids Struct 2003;40:6723–65.
[36] Cline J, Love B. The effect of in-plane shear properties on the ballistic performance of polyethylene composites. Int J Impact Eng 2020;143:103592.